Chapter 2
Transfer of Fluids, Gases and Ions in and Through Cracked and Uncracked Composites

Christian Wagner, Volker Slowik, Gideon P.A.G. van Zijl, William P. Boshoff, Suvash C. Paul, Viktor Mechtcherine and Koichi Kobayashi

Abstract The durability of strain-hardening cement-based materials (SHCC) is strongly influenced by the transport of different substances through the material. Since numerous fine cracks are formed in SHCC, the relationship between the crack pattern and different transport properties has been the subject of experimental investigations, including tests of water and gas permeability, chloride ingress, and capillary absorption. It appears to be insufficient to consider only the average or maximum crack width when transport through SHCC is to be modelled. Therefore, the determination of certain crack pattern parameters has been proposed that take into account both crack widths and distances. These parameters may be linked to certain transport properties of the respective material.

Keywords Transport · Crack patterns · Permeability · Capillary absorption · Chloride ingress

2.1 Introduction

Cracks in concrete members are known to have a significant influence on the transport of fluids, gases and ions through cement-based materials and, thereby, on the structural durability of the respective members. For this reason, crack widths are

C. Wagner (✉) · V. Slowik
Leipzig University of Applied Sciences, Leipzig, Germany
e-mail: christian.wagner@htwk-leipzig.de

G.P.A.G. van Zijl · W.P. Boshoff · S.C. Paul
Stellenbosch University, Stellenbosch, South Africa

V. Mechtcherine
Technische Universität Dresden, Dresden, Germany

K. Kobayashi
Gifu University, Gifu, Japan

G.P.A.G. van Zijl and V. Slowik (eds.), *A Framework for Durability Design with Strain-Hardening Cement-Based Composites (SHCC)*, RILEM State-of-the-Art Reports 22,
DOI 10.1007/978-94-024-1013-6_2

normally restricted by design codes, as, for instance, to about 0.2 mm in ordinary steel-reinforced concrete members. Limits of such an order of magnitude are not acceptable for the fracture behaviour of strain-hardening cement-based materials (SHCC), which is characterised by the formation of a large number of individual cracks with a spacing of only a few millimetres. In order to ensure sufficient durability of such materials, the control and the characterisation of crack patterns appears to be an important goal of durability design.

Knowledge of the transport properties of uncracked SHCC may contribute to the adequate modelling of certain transport mechanisms, but it appears to be impossible to evaluate the durability of the material on the basis of these properties alone. This stems from the fact that transport through cracks tends, in general, to occur much faster than that which occurs through the uncracked material. Hence, the combined action of mechanical loading and exposure to media that might be transported through the cracked material requires consideration.

Most of the reported investigations into transport through cement-based materials have, to date, focused on water as the transport medium. The reason for this focus is that water may directly affect the material properties of the SHCC while also being the transport medium for ions which might be potentially damaging. Hence, the resistance of cracked SHCC to water transport should be maximised. This may be accomplished by controlling and restricting crack widths or by means of water-repellent treatment (see Wittmann et al. 2012).

Two physical processes are of importance for water transport through SHCC: permeability and capillary absorption. The effects of the cracks on these processes are different. Some typical experimental observations and proposed models for the two above-mentioned — and other — transport processes are explained further on in this chapter. The next section, however, is dedicated to the definition and determination of crack pattern parameters that will later be linked to the transport properties.

2.2 Crack Pattern Characterisation

The evaluation of test results that expectedly depend on crack patterns appears to be a challenging task. In repeated tests, it has proved to be impossible to reproduce identical crack patterns concerning crack density, crack width distribution, and crack spacing distribution. Furthermore, it has become apparent that neither the maximum crack width, nor the average crack width may be exclusively used for the evaluation of transport properties. The inability results from the non-proportional influence of the crack width and other crack pattern-related parameters on the transport properties. The strain level is also not directly connected to the transport properties, since the resulting crack pattern depends both on the material properties and on the particular loading conditions involved. Instead, it is proposed to base the estimation of the transport properties on the crack patterns actually observed at the surface of test specimens or structural members. The crack patterns should then be

characterised by considering, in addition to the number of cracks, the crack width distribution and also, especially in the case of capillary absorption, the crack spacing distribution.

With respect to the durability of SHCC, the crack widths are of utmost importance. Their critical nature relies on them having a disproportionate influence on the transport rate for several transport mechanisms, as well as on them also affecting the self-healing potential of the cracks concerned. The number of cracks per unit length, which is a property that is also referred to as crack density, normally has a linear influence on the transport rate involved. In the case of capillary absorption, the individual crack distances also influence the transport rate, especially when the distances concerned are small. The uncracked material between neighbouring cracks absorbs water, but only until the space between them is fully saturated. Therefore, the crack spacing distribution has to be considered, in the case of capillary absorption, as being a third property of the crack pattern. The variation of the crack depths is not considered in the following discussion of crack pattern parameters, since the crack observation is currently almost exclusively undertaken at the surface of SHCC samples. For the durability of real structures, however, crack depths are highly significant.

Prior to the characterisation of crack patterns, they require to be documented, with the cracks involved requiring identification, and the measuring of their widths. This is usually accomplished by means of such non-contact observation methods as digital image processing (DIP), or digital image correlation (DIC). Adequate techniques are explained and compared by Van Zijl et al. (2016), who report on a comparative mechanical test series initiated by the RILEM (International Union of Laboratories and Experts in Construction Materials, Systems and Structures) Technical Committee 208-HFC, Subcommittee 2. As indicated in Chap. 1, five laboratories participated in the study concerned. The purpose of the tests conducted was to compare and discuss experimental observations in terms of crack widths and spacing, and to make recommendations for a suitable test set-up and procedure towards characterising crack patterns on SHCC surfaces.

The characterisation of crack patterns requires the derivation of certain quantitative measures, so as to allow for the making of comparisons and further evaluations. Boshoff and Adendorff (2010) proposed a crack pattern evaluation method with respect to the durability of SHCC, with the method in question considering both the crack width distribution and the number of cracks present. The method yields a single dimensionless numerical value of which the use was recommended in respect of the estimating of the damage potential of cracked SHCC. An advanced version of the method identified has been presented by Boshoff et al. (2016). It also yields single numerical values, characterising the ingress potential of different deleterious materials in cracked SHCC. Due to the high impact of the cracks on the transport mechanisms involved, the transport through the uncracked matrix has been neglected (Boshoff et al. 2016). First, the so-called crack ingress potential (*CIP*) is determined that defines the relative significance of the ingress into a single crack, due to a particular transport mechanism. The relationship between the *CIP* and the crack width has to be based on experimental investigations into the

respective transport mechanism. Examples for the *CIP* are given by Boshoff et al. (2016) for water permeability, based on the experimental results of Wang et al. (1997), and for chloride diffusion, based on experimental results of Djerbi et al. (2008). The following equations apply.

For water flow:

$$CIP = 4.84 \cdot 10^{-17} w_c^{5.62} \tag{2.1}$$

For chloride diffusion:

$$CIP = \begin{cases} 0 & \text{for } w_c \leq 30\,\mu\text{m} \\ 4.115 \cdot 10^{-11} \cdot w_c^2 - 1.235 \cdot 10^{-15} \cdot w_c & \text{for } 30\,\mu\text{m} < w_c \leq 100\,\mu\text{m} \\ 2.881 \cdot 10^{-15} \cdot w_c & \text{for } w_c > 100\,\mu\text{m} \end{cases} \tag{2.2}$$

Expectedly, the *CIP* increases with the crack width w_c. The *CIP* is then used for weighting the crack width distribution. For the latter, a log-normal probability density function is adopted:

$$f(w_c) = \frac{1}{w_c \sqrt{2\pi\sigma}} \mathrm{e}^{\frac{-(\ln(w_c)-\mu)^2}{2\sigma^2}} \tag{2.3}$$

with the parameters μ and σ.

The above yields the so-called *IPD*.

For water flow:

$$IPD = \frac{4.84 \cdot 10^{-17} \cdot w_c^{5.62}}{w_c \sqrt{2\pi\sigma}} \mathrm{e}^{\frac{-(\ln(w_c)-\mu)^2}{2\sigma^2}} \tag{2.4}$$

For chloride diffusion:

$$IPD = \begin{cases} 0 & \text{for } w_c \leq 30\,\mu\text{m} \\ \frac{4.115 \cdot 10^{-11} \cdot w_c^2 - 1.235 \cdot 10^{-15} \cdot w_c}{w_c \sqrt{2\pi\sigma}} \mathrm{e}^{\frac{-(\ln(w_c)-\mu)^2}{2\sigma^2}} & \text{for } 30\,\mu\text{m} < w_c \leq 100\,\mu\text{m} \\ \frac{2.881 \cdot 10^{-15} \cdot w_c}{w_c \sqrt{2\pi\sigma}} \mathrm{e}^{\frac{-(\ln(w_c)-\mu)^2}{2\sigma^2}} & \text{for } w_c > 100\,\mu\text{m} \end{cases} \tag{2.5}$$

Finally, the *IPD* is integrated over the crack widths and multiplied by the so-called crack intensity C_i. This yields the Ingress Potential Index (*IPI*) as a single dimensionless numerical value:

$$IPI = C_i \int_0^\infty IPD \, dw_c \tag{2.6}$$

with $C_i = \frac{\text{number of cracks per metre}}{1000}$

Figure 2.1 shows, for a certain example, the unweighted and weighted probability density functions of the crack width at different strain levels, as well as the *IPI* for chloride diffusion and water flow (Boshoff et al. 2016). Due to the weighting by the *CIP* for water flow (see Fig. 2.1b), the larger cracks might be seen to have a more significant impact on the ingress potential than do the smaller ones. Figure 2.1c shows that the two transport mechanisms considered here exhibit different strain dependencies.

It has to be taken into account that the *IPI* values for different transport mechanisms cannot be directly compared because of the independent normalizations involved. Currently, the concept does not allow for the quantitative derivation of a flow rate, or of an absorbed water volume, for a certain crack pattern under a given exposure. In addition, the interaction between neighbouring cracks is not yet considered, with the crack spacing distribution not yet being an input parameter. In the case of water permeability, the above is not expected to cause significant error, but, in the case of capillary absorption, the individual crack distances are of importance (see Sect. 2.6).

Motivated by the work of Boshoff and Adendorff (2010), an alternative method of crack pattern evaluation was developed by Wagner (2016), Wagner and Slowik (2011), and Wagner et al. (2011, 2012). The main advantage of the newly

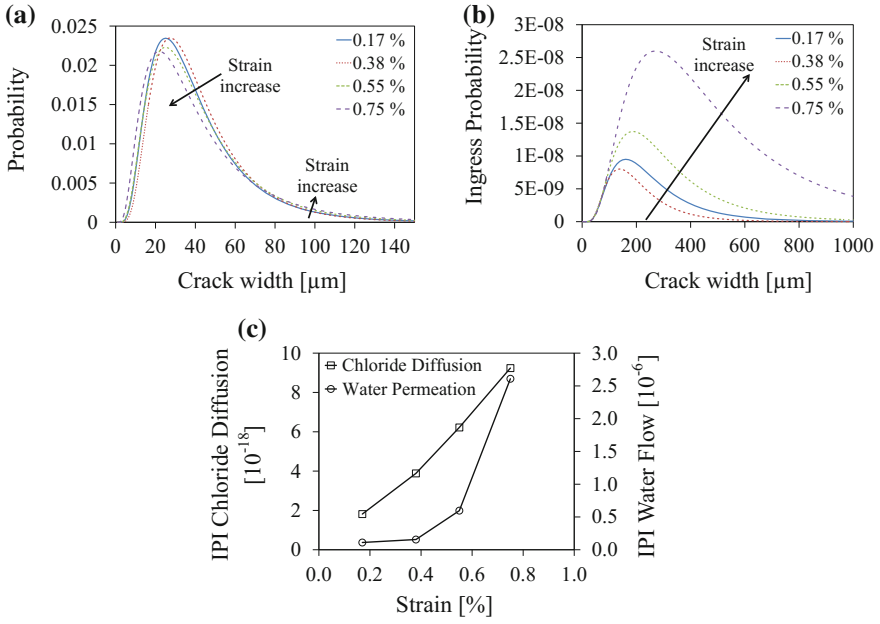

Fig. 2.1 **a** The unweighted and **b** weighted (*IPD* for water flow) probability density functions of the crack width at different strain levels, and **c** the Ingress Potential Index (*IPI*) for chloride diffusion and water flow (reproduced from Boshoff et al. 2016)

developed approach is the physically justified and quantitative linking of adequate crack pattern parameters to certain transport properties, for instance to the water flow in m^3/s, or to the capillary absorption in kg/m^2. Such linking enables a comparison to be drawn with allowable or acceptable values. Due to the different transport mechanisms, different crack pattern parameters are proposed for permeability and capillary absorption, respectively, although, in each case, they are expressed as a single numerical value.

As a prerequisite, it is necessary to present the measured crack width distributions as so-called crack width polygons (*CWP*) (see Fig. 2.2). The format of the curves resembles that of grain-size distribution curves. For the respective crack pattern, the percentage of cracks with certain widths is cumulated. This method of presentation allows for the quick determination of the percentage of cracks, the width of which does not exceed a certain limit. The residual strain, as indicated in Fig. 2.2, is the sum of the crack widths in the unloaded specimen related to the evaluation length. Deformations of the material between the cracks are not considered. Note that the *CWP* is completely independent of the crack density, i.e., of the number of cracks.

On the basis of the *CWP*, the so-called crack width value (*CWV*) may be determined by adding the complements of the frequency values for all crack width classes i:

$$CWV = \frac{\sum_{i=0}^{n}(100 - CWP(w_i))}{100} \tag{2.7}$$

It has to be taken into account that the *CWV* depends on the class width Δw of the crack width distribution. For a constant Δw, the product $(CWV \cdot \Delta w)$ yields the average crack width. The major advantage of assigning the individual cracks to certain classes and of deriving the *CWV* is the opportunity to weight each class according to certain transport mechanisms (see Sect. 2.3). In previous publications by Wagner and Slowik (2011) and Wagner et al. (2011, 2012), the symbol *CCV* (for cumulated crack width value) has been used, instead of *CWV*. The reason for

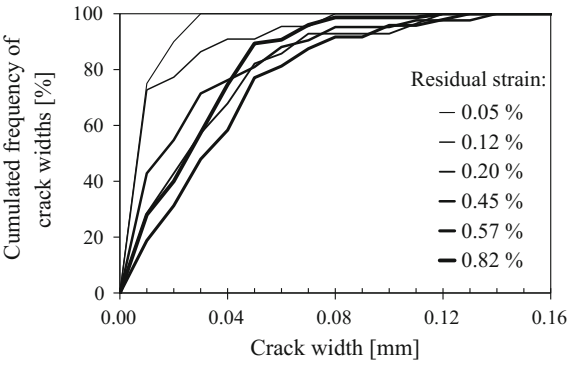

Fig. 2.2 Crack width polygons (*CWP*) for six damage levels, as expressed by the residual strain (Wagner and Slowik 2011)

the name change was the intended consistency of the notation for different crack pattern parameters.

In an analogy in reference to the crack width value (*CWV*), a crack spacing value (*CSV*) and a crack length value (*CLV*) may be determined.

$$CSV = \frac{\sum_{i=0}^{n}(100 - CSP(w_i))}{100} \tag{2.8}$$

$$CLV = \frac{\sum_{i=0}^{n}(100 - CLP(w_i))}{100} \tag{2.9}$$

with: *CSP* the crack space polygon
CLP the crack length polygon

The crack density (*CD*), meaning the number of cracks per unit length, also requires consideration when evaluating crack patterns with respect to the transport properties involved. Table 2.1 shows examples of the crack pattern characterisation by the proposed method. Assuming that the observed cracks completely split the specimens concerned, the *CLV* is constant for each series and, when multiplied by the class width Δl, it yields the specimen width. The values in the three lines at the bottom of Table 2.1, which are required for modelling water permeability, will be explained in Sect. 2.3.

2.3 Water Permeability

The pressure gradient-induced water transport in SHCC is dominated by the flow through the cracks, with the contribution of the material between the cracks being of minor importance. Such dominance stems from the comparatively high flow rate through the cracks, which can be described in terms of the Hagen–Poiseuille equation:

$$Q_t = \frac{\Delta p \cdot w^3 \cdot l}{d \cdot 12 \cdot \eta} \tag{2.10}$$

with:

Q_t theoretical flow rate (m^3/s)
Δp pressure difference (Pa)
w crack width (m)
l crack length (m)
d specimen thickness (m)
η dynamic viscosity (Pa·s)

The theoretical flow rate Q_t is a maximum value that is based on the assumption of laminar flow between smooth parallel-sided and continuous planes. The value

Table 2.1 Crack pattern parameters of selected samples and the corresponding normalised theoretical water flow rates

						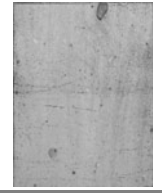
Series	1	4	1	4	1	4
Residual strain (%)	0.12	0.10	0.48	0.45	0.65	0.60
CD (cracks/m)	35	55	111	83	99	189
CWV (−) $\Delta w = 0.01$ mm	2.0	2.3	4.8	6.0	7.0	3.8
CSV (−) $\Delta s = 1.0$ mm	9.1	15.2	8.5	10.9	9.4	5.4
CLV (−) $\Delta l = 10$ mm	4.0	6.0	4.0	6.0	4.0	6.0
CWV_{WP} (−)	264	61	292	639	2077	123
R_{WP} (mm^3•cracks/m)	0.0091	0.0034	0.0326	0.0533	0.2056	0.0233
$Q_{t,normalised}$ (−)	1.00	0.36	3.56	5.71	22.48	2.50

concerned is unreachable in real materials. The influence of all flow-reducing effects is considered in terms of a flow coefficient ξ_{WP} that relates the measured flow rate Q_m to the theoretical flow rate Q_t.

$$\xi_{WP} = \frac{Q_m}{Q_t} \tag{2.11}$$

Note that the proportionality of the theoretical flow rate to the third power of the crack width points to the importance of limiting crack widths in the durability design of SHCC members. When, for example, a crack of width 0.2 mm is replaced by four fine cracks of width 0.05 mm, the theoretical flow rate is reduced by 93.75%.

Experimental investigations into the water permeability of SHCC were reported by Lepech and Li (2009). The measured flow rates were related to the maximum crack width, and to the tensile strain. The average crack width did not exceed 70 µm, up to a tensile strain of 3%. Reference permeability tests with steel-reinforced mortar revealed that the SHCC had a six orders of magnitude smaller water permeability.

Mechtcherine and Lieboldt (2011) conducted permeability tests of cracked textile-reinforced concrete. Concerning the crack pattern created under tension, similarities exist between such a type of material and SHCC. It could be shown that the transport rate overproportionally increases along with the tensile strain. This observation may be attributed to the increasing crack widths involved. The measured flow rate was compared to a calculated one based on the Hagen–Poiseuille equation, whereby the flow coefficient ξ varied between $0.28 \cdot 10^{-3}$ and $0.75 \cdot 10^{-3}$. Furthermore, it was observed that the self-healing of fine cracks significantly reduced the water permeability concerned over time.

Wagner (2016) conducted water permeability tests of pre-cracked SHCC specimens. The specimens were cut out of preloaded dumbbell-shaped specimens of a length of 310 mm, with the inner part having a length of 100 mm, and a constant cross-section (see Fig. 2.3). The specimens were subjected to uniaxial tension up to certain strain levels (0.25, 0.50, 1.00, 1.50%). Thereafter, the specimens were unloaded, with the inner part then being used for permeability and capillary absorption tests.

Prior to the permeability tests, the crack patterns on the front and back of the unloaded specimens were photographically documented and evaluated. Thereafter, the side faces of the specimens were sealed, so as to allow for one-dimensional transportation during the permeability tests. When 28 days old, the unloaded specimens were, first, water stored and then, on one side, subjected to water pressure. In previous permeability tests of cracked steel-reinforced concrete, such as those published by Edvardsen (1996), pressure gradients of up to 0.5 MPa/m were applied. Such a value is realistic for the usual concrete members with thicknesses of at least 25 cm. In thin repair layers, however, significantly higher pressure gradients of more than 5 MPa/m can occur. Mechtcherine and Lieboldt (2011) performed permeability tests with pressure gradients of the same order of magnitude (i.e.

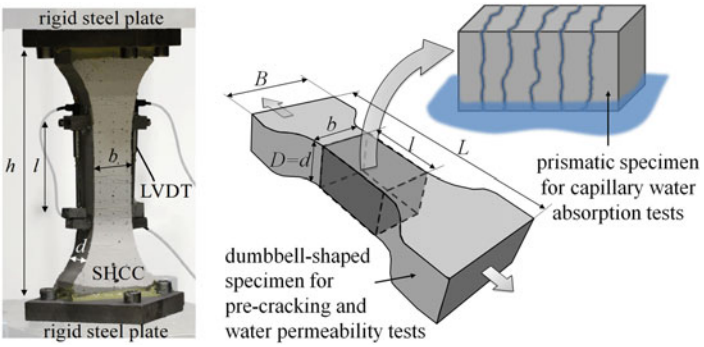

Fig. 2.3 Pre-cracking of specimens for permeability and capillary absorption tests (Wagner 2016)

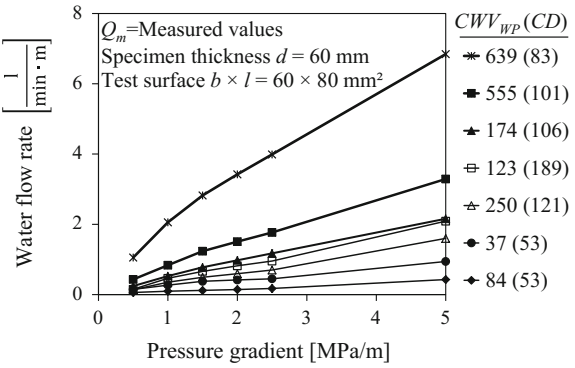

Fig. 2.4 Water flow rate, as dependent on the pressure gradient (Wagner 2016)

12.5 MPa/m) in cracked textile-reinforced concrete. In the experiments described in the current chapter, the applied pressure gradients ranged from 0.5 to 5 MPa/m. In addition to the pressure gradient and to the damage level expressed by the residual strain after pre-cracking, the specimen thickness was also varied. Figure 2.4 presents the results of one particular test series (Wagner 2016). The figure shows the water flow rate versus the pressure gradient for different damage levels, i.e., for different residual strains after pre-cracking and unloading. Each curve represents the behaviour of one particular specimen, with its unique crack pattern. The water flow rates in l/(min·m) presented in the diagrams in the present section are given per unit width, with them having been normalised to the same specimen thickness.

The evaluation of the results presented in Fig. 2.4 revealed a problem associated with the strain values used for characterising the damage level. As no clear dependency between flow rate and residual tensile strain could be identified, it appeared to be necessary to relate the water flow rate not to a strain value, but to

certain crack pattern parameters. Such an approach will be followed later on in the present section.

In order to provide test conditions that realistically resembled real SHCC applications, Wagner (2016) conducted additional tests at SHCC overlays on concrete substrate with artificial crack (see Fig. 2.5). For creating cracks in the SHCC overlays, so-called zero-span elongation tests were conducted (Fig. 2.5a). The respective specimens consisted, in each case, of two concrete cuboids ($70 \times 70 \times 75$ mm^3) that were placed on top of each other, with the joint between the cuboids serving as an artificial crack. By means of displacing the cuboids, the artificial crack could be opened, or closed. The SHCC layers, which had been applied to two opposite side faces of the cuboids in question, were locally stressed when the artificial crack was opened. In Fig. 2.5a it can be seen that the wide-opened artificial crack between the cuboids did not 'break through' the SHCC overlay. The latter is also cracked, but with numerous fine cracks, rather than with a single crack.

The principle of the permeability tests at the pre-cracked SHCC overlays is shown schematically in Fig. 2.5b. In the loaded state, spacers had been placed between the two concrete cuboids so as to keep the artificial crack open during the subsequent permeability test. Despite the intended symmetrical preloading, different crack patterns were formed in the overlays on the two opposite sides of the concrete cuboids serving as substrate. Therefore, the crack patterns were documented and characterised on both surfaces. The parallel side faces of the samples were sealed so as to force the flow through one of the SHCC overlays and part of the artificial crack. Figure 2.6 shows the measured water flow rate versus the pressure gradient for an SHCC layer with a thickness of 20 mm. The individual curves, corresponding, in terms of their crack patterns, to certain specimens, exhibit a deviation from proportionality that is contradictory to the prediction of the Hagen–Poiseuille equation. This may be attributed to a deviation from laminar flow conditions, as

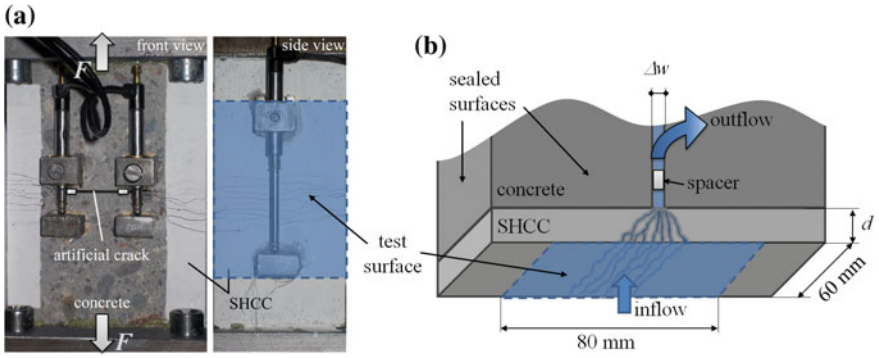

Fig. 2.5 **a** Pre-cracking of the SHCC overlay, and **b** the permeability test (Wagner 2016)

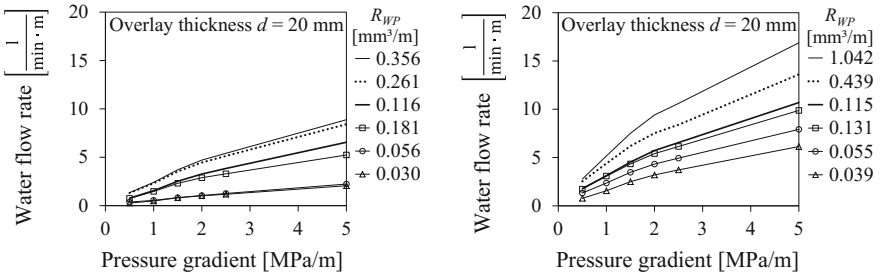

Fig. 2.6 Water flow rate, as dependent on the pressure gradient for an SHCC layer thickness of 20 mm (Wagner 2016)

well as to other flow-reducing effects, as, for instance, the particle plugging of cracks. It was also found that the flow rate appears not to be directly related to an overall strain value, which, in the present case, would be dependent on the artificial crack opening. Again, this observation points to the necessity to relate the permeability to the actual crack pattern parameters involved.

In the following, a method is proposed that links the water permeability to the crack pattern (Wagner 2016; Wagner and Slowik 2011). The pressure gradient-induced water flow rate depends on the crack density (*CD*), specifically on the number of cracks per unit length, and on the crack width distribution. The latter is highly relevant, due to the above-mentioned predominant effect of the crack width on the water flow rate. It can be expressed by means of the crack width value (*CWV*) calculated on the basis of the crack width polygon (*CWP*). However, it is necessary to weight each class of crack widths with respect to its influence on the water permeability. An adequate weighting function for this particular transport mechanism $W_{WP}(i)$ has been derived on the basis of the Hagen–Poiseuille equation (Wagner 2016):

$$W_{WP}(i) = 3i^2 + 3i + 1 \tag{2.12}$$

Using the function stated, the crack width value CWV_{WP} weighted for water permeability is obtained, as follows:

$$CWV_{WP} = \frac{\sum_{i=0}^{n} W_{WP}(i) \cdot (100 - CWP(w_i))}{100} \tag{2.13}$$

The *CWV* has to be considered as generally depending on the chosen class width Δw.

The theoretical water flow rate Q_t may now be calculated as follows:

$$Q_t = \frac{\Delta p \cdot b \cdot l \cdot \Delta w^3}{d \cdot 12 \cdot \eta} \cdot CWV_{WP} \cdot CD \tag{2.14}$$

with:

b	evaluation length
Δw	chosen class width for the CWP
CWV_{WP}	weighted crack width value
CD	crack density

All other symbols were introduced with the provision of the Hagen–Poiseuille equation (see above). The product $b \cdot CD$ yields the total number of cracks. All crack pattern dependent influences on the theoretical flow rate Q_t may be combined and expressed by means of a so-called hydraulic crack pattern parameter R_{WP}. Doing so facilitates the evaluation of observed crack patterns, as well as their comparison with respect to structural durability.

$$R_{WP} = \Delta w^3 \cdot CD \cdot CWV_{WP} \tag{2.15}$$

On the basis of the hydraulic crack pattern parameter R_{WP}, the flow rate may be predicted more reliably than on the basis of the irreversible strain. This is demonstrated in Fig. 2.7, in which the flow rate that was measured by Wagner (2016) in uniaxially pre-cracked specimens, is plotted versus the irreversible strain (Fig. 2.7a), and versus the hydraulic crack pattern parameter R_{WP} (Fig. 2.7b). In the last-mentioned case, a better correlation is obtained than in the previous one.

Corresponding results for the SHCC overlays on concrete substrate with artificial crack are presented in Fig. 2.8. As in the previous case, a better correlation is obtained if the flow rate is plotted versus the hydraulic crack pattern parameter R_{WP}.

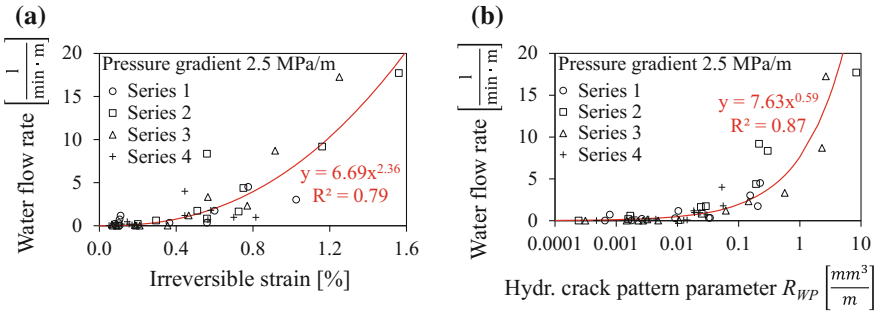

Fig. 2.7 Water flow rate measured by Wagner (2016) in uniaxially pre-cracked specimens, versus **a** the irreversible strain, and versus **b** the hydraulic crack pattern parameter R_{WP}

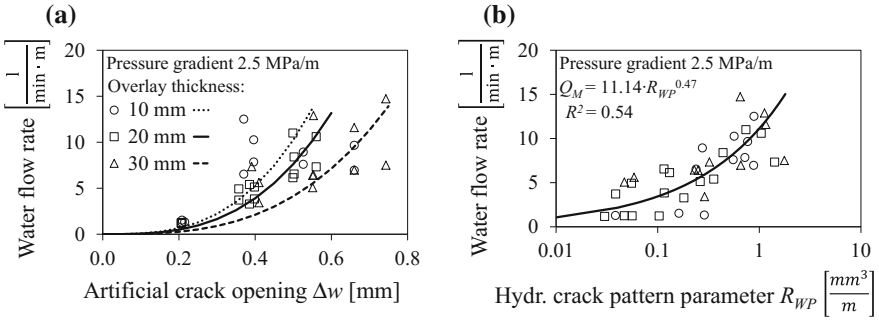

Fig. 2.8 Water flow rate measured by Wagner (2016) at the SHCC overlays, versus **a** the artificial crack opening, and versus **b** the hydraulic crack pattern parameter R_{WP}

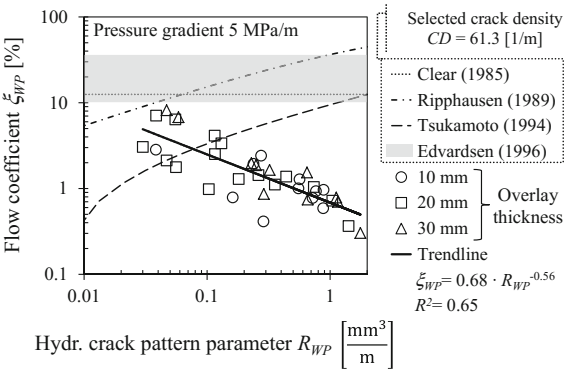

Fig. 2.9 Flow coefficient ξ_{WP} versus the hydraulic crack pattern parameter R_{WP} with Wagner's (2016) experimental results being compared to those of other authors

In Fig. 2.8a, the influence of the overlay thickness can be seen. Functions $Q = A \cdot w^3$ were fitted to the measured data. Expectedly, a clear trend of reduced permeability for thicker overlays exists, despite the comparatively large scatter when the artificial crack opening serves as abscissa.

Figure 2.9 shows the flow coefficient ξ_{WP} as being dependent on the hydraulic crack pattern parameter R_{WP}. As explained before, this coefficient is the ratio of measured and theoretical flow rate. Wagner's (2016) experimental results are compared to the results that have been reported by other authors for different cement-based materials. The opposite trend found by Wagner (2016) represents a material-specific behaviour of SHCC that is mainly attributed to the characteristic crack width distribution, which is expressed in the given instance by means of the weighted crack width value CWV_{WP}.

2.4 Gas Permeability

Very little information is available on the air permeability of cracked SHCC. Mechtcherine et al. (2007) reported on permeation tests performed on uncracked and cracked SHCC specimens (Ø 100 mm, height of 60 mm) cored from dumbbell-shaped prisms. Figure 2.10 shows the cracked cored specimens and a schematic view of the test set-up used for the air permeability measurements.

The obtained results indicate that the air permeability of uncracked SHCC is within the range of typical values for ordinary concrete. When the material is loaded up to a tensile strain of 0.5%, an increase of almost two orders of magnitude has been observed (Mechtcherine et al. 2007) (see Fig. 2.11). Whereas such values are

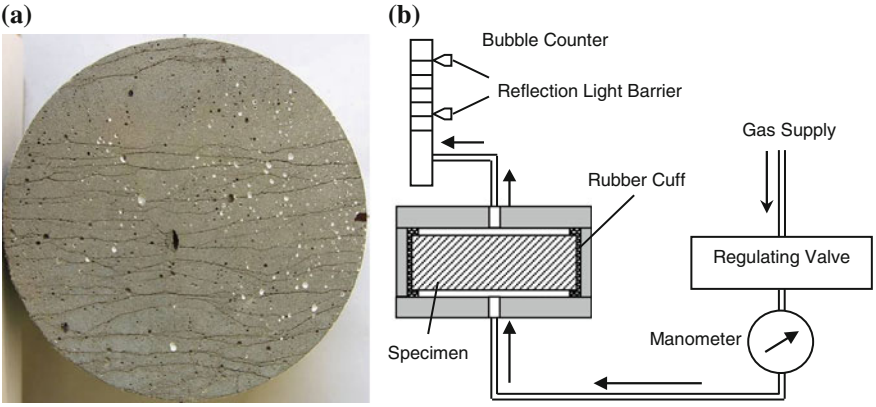

Fig. 2.10 **a** Cylindrical test specimen (cracked) cored from prism tested to failure under monotonic loading (ε = 6.5%), **b** schematic view of the test set-up used for air permeability measurements

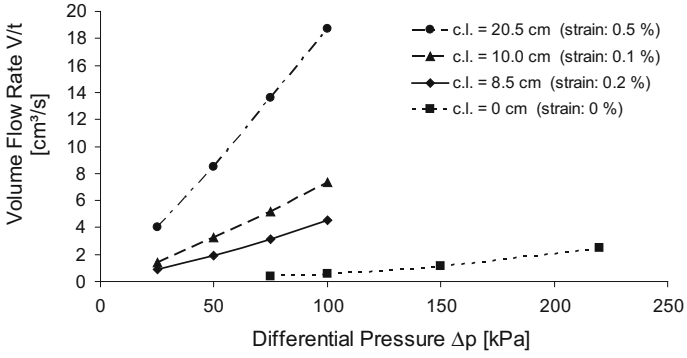

Fig. 2.11 Air volume flow rate as a function of differential pressure for selected specimens with different residual strain levels, with c.l. being the cumulative crack length (Mechtcherine et al. 2007)

no longer comparable to those of sound concrete, it should be noted that the specimens were tested at an age of 45–50 days, and that the mix had a high content of fly ash. Thus, it can be expected that, in field applications with similar mixes, ongoing hydration and self-healing should have a mitigating influence over time.

Whereas all crack widths present were found to be smaller than 0.1 mm, their number varied significantly and generally increased with increasing strain level. To quantify the pre-damage, the cumulative crack length was measured for each specimen. Only pass-through cracks were considered, meaning cracks going completely through the specimen. Figure 2.12 shows all results of the air volume flow measurements at a pressure difference of 50 kPa. A pronounced linear correlation between volume flow rate and cumulative crack length was found for the considered strain range from 0 to 1%.

Mechtcherine and Lieboldt (2011) reported on gas permeability tests of cracked textile-reinforced concrete. As previously stated, the crack patterns created in the

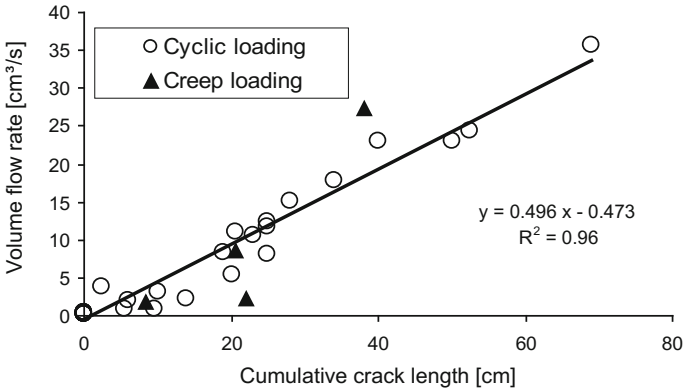

Fig. 2.12 Effect of the cumulative crack length on the air volume flow rate, cylinders with Ø 100 mm and height of 60 mm, differential pressure 50 kPa, room temperature (Mechtcherine et al. 2007)

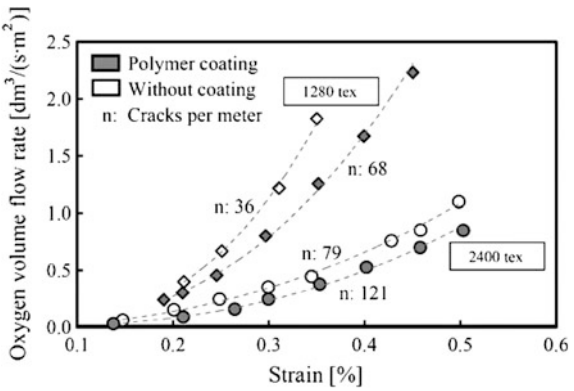

Fig. 2.13 Oxygen flow rate in cracked textile-reinforced concrete under increasing tensile strain, at a pressure difference of 3 kPa (Mechtcherine and Lieboldt 2011)

type of material mentioned are similar to those found in SHCC. Figure 2.13 shows the oxygen flow rate measured in a permeability cell under uniaxial tension at a pressure difference of 3 kPa. Under increasing strain, the crack widths can be seen to be growing larger, resulting in the hyperproportional increase of the flow rate. For the uncoated yarn of a fineness of 1280 tex (see the upper curve in Fig. 2.13), the average crack width in the unloaded state amounted to 65 µm, which is in the order of magnitude of what is expected for SHCC. The other curves correspond to smaller average crack widths.

2.5 Chloride Ingress

Steel corrosion in reinforced concrete (RC) is known to be caused by carbonation or chloride, with models having been proposed for both deterioration mechanisms (DuraCrete 2000). Chloride-induced corrosion in steel-reinforced SHCC (R/SHCC) is described in more detail in Chap. 9. In the current section, chloride ingress is reported for both reinforced and unreinforced SHCC.

2.5.1 Chloride Profile in Cracked and Uncracked SHCC

Kojima et al. (2014) immersed an entire SHCC test specimen, which was pre-cracked, in a 3% NaCl solution for a period of one month, and then, after breaking the test specimen apart, analysed the chloride content in the fracture surface. The results showed that 4 kg/m^3 or more of chloride per unit volume of mortar (i.e. approximately 0.6% or more of the cement mass) had been accumulated in the fracture surface. Such quantity may have caused embedded steel to corrode, if a sufficient amount of oxygen was present. In the case of the penetration of chloride aqueous solution to the interior of cracks, however, the results may differ, depending on the conditions under which the liquid was provided: by spraying; by alternate wetting and drying; or by immersion.

Chloride profiles determined by chemical titration are shown in Fig. 2.14 (Wittmann et al. 2011). Dumbbell specimens were first loaded in a stiff steel test rig. Then, chloride penetration into the specimens under imposed strain was determined by means of a modified Karsten tube. In this case, a surface of 40 × 100 mm^2 was put in contact with a box containing 3.1% NaCl solution. After the contact between the SHCC and the salt solution had been maintained for three hours, thin layers were removed successively from the surface, which had been in contact with the salt solution, by means of milling. The free chloride content of the powder obtained was then determined by titration, according to RILEM TC 178-TMC (2002b). The dumbbell specimens were loaded to predetermined average tensile strains ranging from 0% (uncracked) to 2%. Higher free chloride content was found in the specimens that were loaded to higher average tensile strains. In the cracked specimens,

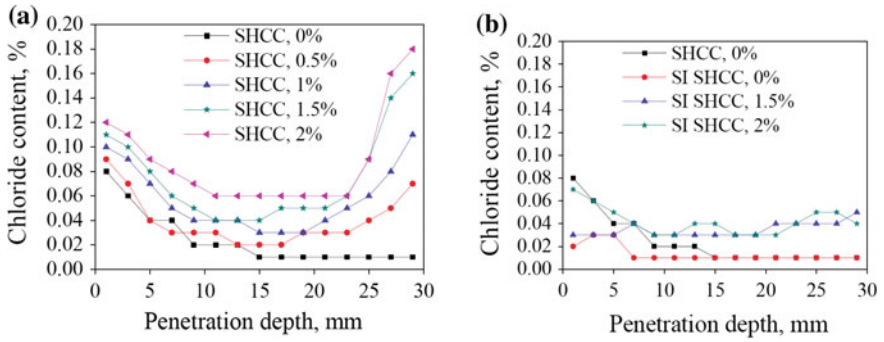

Fig. 2.14 Influence of imposed strain on free chloride profiles in unreinforced, uncracked and cracked SHCC, after contact of one surface with a 3.1% NaCl solution for three hours, showing specimens that were **a** untreated and **b** surface-impregnated with silane emulsion for the purpose of water repellence (Wittmann et al. 2011)

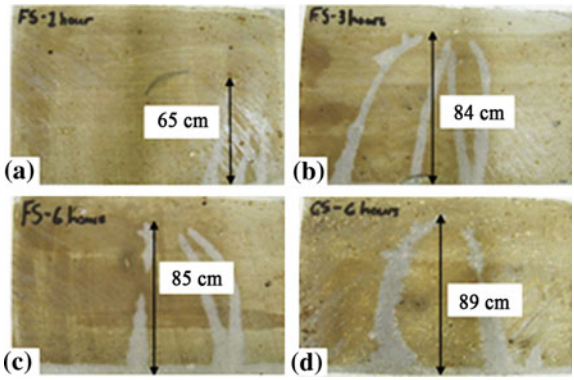

Fig. 2.15 Chloride penetration in 100 mm high, pre-cracked specimens after chloride exposure for **a** 1 h, **b** 3 h, **c** 6 h, and **d** a pre-cracked specimen containing course sand, after chloride exposure for 6 h (Paul and Van Zijl 2014)

significantly higher chloride content was seen at the opposite face of the immersed surface of the specimens, which was ascribed to evaporation at the opposite face causing significant deposits of chloride close to the face concerned (Wittmann et al. 2011). Figure 2.15b shows the free chloride profiles for similar SHCC specimens that were surface-treated with silane emulsion for water repellence.

Typically, in cracked SHCC specimens, the chloride penetration is rapid. In similar capillary absorption tests performed by Paul and Van Zijl (2014) on SHCC specimens that were pre-cracked in bending, chloride reached the full crack depth within one to three hours and, subsequently, the chloride penetrated from the crack faces into the matrix, as is shown in Fig. 2.15. The grey-white coloured areas show the areas to which chloride had penetrated, as prepared by silver nitrate spraying of the inner surface, which was exposed by cutting the specimen after the chloride absorption had taken place. The width of the cracks in the unreinforced SHCC was in the range of 50–100 μm. As the figure shows, in one to 6 h after the bottom of

the test specimen had been immersed in a 3.5% NaCl solution, the chloride had penetrated to a depth of several centimetres along the cracks.

The total chloride content (% by weight of binder) profile was also determined for cracked steel-reinforced SHCC specimens subjected to cyclic wetting (three days) and drying (four days) exposure to 3.5% NaCl solution by means of capillary absorption and ponding, respectively (Paul 2015). Cyclic wetting and drying exposure to NaCl solution allows for the relatively deep penetration of chloride ions (Moukwa 1990), and it can lead to corrosion rates in RC that are 20 times higher than are those resulting from exposure to a continuous salt fog (Yeomans 2004). The material composition for the SHCC specimens tested by Paul (2015) is shown in Table 2.2. FS2, CS2, and FS31 specimens (nominally 100 × 100 × 500 mm^3) were pre-cracked in three-point bending. In Series 1 (FS2, CS2), the specimens were unloaded after flexural cracking and subsequently exposed to cyclic wetting by means of capillary absorption and drying, meaning in the unloaded condition. In Series 2 (FS31), the specimens were also cracked in three-point bending, but then retained in special steel frames and subjected to cyclic ponding of the salt solution, meaning in the loaded condition. It should be noted that the specimens were loaded either to, or close to, their maximum capacity, so as to maximise crack widths for the current study. The full details of the crack widths that were recorded on the farthest tensile face are given in Paul (2015). The surface crack widths ranged between 0.02 and 0.25 mm, but with average widths in the range of 0.02–0.06 mm for the unloaded specimens (Series 1, FS2 and CS2), and between 0.02 and 0.25 mm applying in the case of the loaded specimens (Series 2, FS31), with their average crack widths being in the range of 0.03–0.17 mm. All the cracks formed in a central 200 mm long zone of the 500 mm long specimens. Series 1 was subjected to 88 weeks of cyclic absorption, with only the 200 mm central, cracked face being exposed to salt solution. In contrast, Series 2 was subjected to 37 weeks (with some up to 57 weeks) of cyclic ponding on the cracked central 200 mm length.

The chloride profiles shown in Fig. 2.16 for the cracked steel-reinforced SHCC specimens were determined by means of the X-ray fluorescence (XRF) method. In the present case, the powder samples were collected by means of drilling from the exposed surface in layers of 3 mm each, down to a depth of 45 mm in the specimens. A drill with diameter of 16 mm was used at four to six cracked positions to ensure that there was sufficient powder per layer. So, the chloride content obtained in the instance mentioned is the average value of different cracked positions within

Table 2.2 Amount of materials (kg/m^3) used in SHCC mixes (Paul 2015)

Type	Id	Cement	Fly ash	Sand	Water	PVA fibre
SHCC	Series 1: FS2, CS2[a]	392	674	553	392	2%
	Series 2: FS31					
	Series 3: FS32[b]					

[a]Note that the maximum aggregate size in the present case was 1.7 mm, whereas in others it was 0.25 mm

[b]Series 3 is discussed in Sect. 9.3

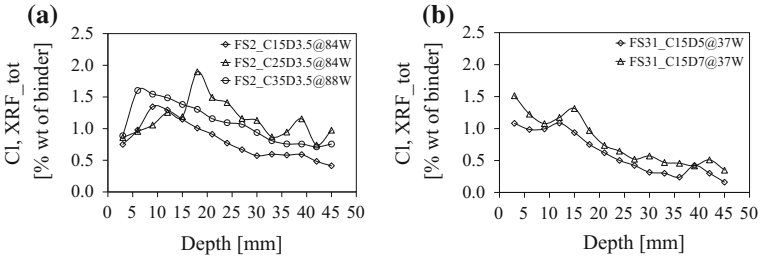

Fig. 2.16 Total chloride content determined by XRF after different periods of **a** capillary absorption and **b** ponding exposures in cracked steel-reinforced SHCC specimens (reproduced from Paul et al. 2016)

a single layer. Note further that different cover depths of the steel (15, 25 and 35 mm, as denoted by C15, C25, C35 in Fig. 2.16) were used, and that the bending tests were performed up to different deflection levels (3.5, 5 and 7 mm, as denoted by D3.5, D5, D7 in Fig. 2.16). The chloride profiling was done after a varying number of weeks, ranging from 37 weeks up to 88 weeks, as seen in the legend of Fig. 2.16. From Fig. 2.16, it is clear that significantly (an order of magnitude) higher chloride content was found than in cracked specimens of Fig. 2.14 that were subjected to absorption for only three hours.

Kobayashi et al. (2010) reported chloride penetration, as can be seen in Fig. 2.17, in cracked RC beams (of size 40 × 100 × 1800 mm^3) in which cracking

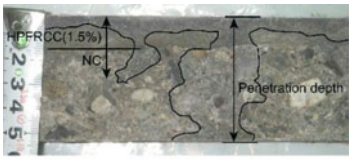

a HPFRCC surface-coated specimen

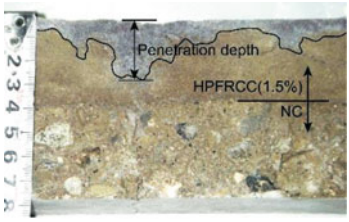

b HPFRCC-patched specimen

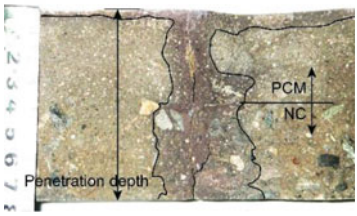

c PCM-patched specimen

Fig. 2.17 Examples of chloride penetration profiles in HPFRCC specimens (Kobayashi et al. 2010)

was introduced by uniaxial tensile loading, up to a crack width of about 0.40 mm. In the present case, two steel reinforcing bars were used in the beams, with a cover depth of 25 mm, and with the 150 mm long specimens being cut out from the cracked part of the 1800 mm long beams. Before forming the cracks, the surface of the RC specimens was treated in three different ways: (a) a 10 mm layer of high-performance fibre-reinforced cement composite (HPFRCC) above the steel bars was applied to act as a surface coating to the specimen; (b) a 35 mm layer of HPFRCC was used to cover the steel bars of the patched specimen; and (c) a 35 mm layer of polymer cement mortar (PCM) was overlaid on the RC surface covering the steel bars of the patched specimen. The HPFRCC was reinforced with high-strength polyethylene (PE) fibres. The volumetric fibre content ranged from 0.75 to 1.5%, with only results for 1.5% being presented in Fig. 2.17. For chloride penetration, a 3% sodium chloride aqueous solution was sprayed for a period of 60 days. The spraying was conducted for a period of 5 min every 6 h. The coloured areas indicate the areas where chloride ions penetrated, as visualised by silver nitrate spraying. A comparison of Figs. 2.15 and 2.17 clearly shows that (i) the chloride penetration depth in SHCC at locations other than cracked locations was small; (ii) in test specimens (a) and (c), as shown in Fig. 2.17a, c, chloride penetrated to the interior through the cracks; and (iii) in the concrete, the chloride penetration depth from the cracks in the normal direction to the cracks is relatively large. SHCC, used as patch repair (Fig. 2.17b), showed excellent reinforcement corrosion-resistant performance in the tests undertaken in this regard, as will be discussed in Chap. 9.

For allowing strain-hardening behaviour based on the properties of PE fibres, the mortar matrix that was used in the study by Kobayashi et al. (2010) had a high strength, with a low water–cement ratio (w/c = 0.3). In contrast, the fibres used in the study by Paul (2015) were made of polyvinyl alcohol (PVA), and the w/c ratio was higher than the ratio mentioned above. In order to achieve pull-out of the fibres concerned under tensile stress, although the mortar matrix had a large powder content, a large quantity of fly ash was used in the mix, resulting in a w/c of 1.0 and a w/b of 0.37, if all the fly ash involved were considered as binder.

2.5.2 Total and Free Chloride Content in SHCC

The total and free chloride content in SHCC was determined by Paul (2015) by means of chemical titration, according to RILEM TC 178-TMC (2002a, b) recommendations. It is argued that not all the chloride in concrete contributes to the corrosion process. Some of the chloride binds with the paste present. The unbound, or free, chloride in concrete is believed to participate in the corrosion process. However, some of the bound chloride may dissolve over time and also participate in the corrosion process. This complex process involves many factors, such as the temperature, the relative humidity, the moisture content, the amount of binder content, and the microstructure of the concrete. For the particular mix design of

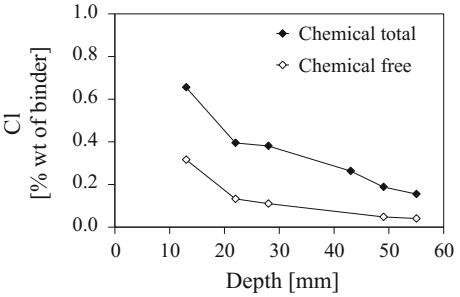

Fig. 2.18 Total and free chloride content in a precracked specimen of Series 3 (Table 2.2), after seven days of continuous ponding (reproduced from Paul et al. 2016)

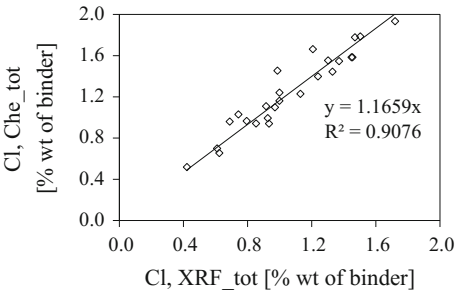

Fig. 2.19 Relationship between the XRF and the chemical analysis of total chloride content (reproduced from Paul 2015)

SHCC that is shown in Table 2.2, the free and total chloride contents from the chemical analysis are shown in Fig. 2.18. The ratio of free to total chloride content was found to be smaller at greater depths in the cracked reinforced SHCC.

Figure 2.19 shows the correlation between the total amount of chloride that was obtained by means of chemical analysis and that which was determined by XRF analysis for the same samples, as taken from the chloride-exposed reinforced SHCC specimens (Paul 2015). The strong, direct relationship indicates that XRF total chloride analysis may be an alternative to the chemical analysis concerned. The chemical analysis is significantly more time-consuming than is XRF.

2.5.3 Influence of Crack Patterns on Chloride Content in SHCC

The influence of the average surface crack width (ACW) on chloride penetration in reinforced SHCC was observed by Paul (2015), as is shown in Fig. 2.20. No correlation is seen to exist between crack width and chloride content in Fig. 2.20a. In Fig. 2.20b, it appears that the total amount of chloride increases as the ACW increases from 0.03 to 0.16 mm. Note, however, that although the ACWs are small in Fig. 2.20a, the specimens involved were exposed for a significantly longer period of time (for 108 weeks in total) than were those in Fig. 2.20b (for 57 weeks),

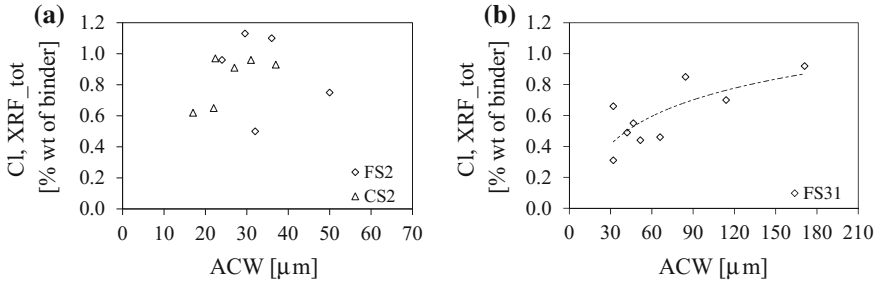

Fig. 2.20 XRF total chloride (Cl) and average crack widths (ACW) relationship in reinforced SHCC specimens, after **a** 108 weeks (Series 1), and after **b** 57 weeks (Series 2) of chloride exposure (reproduced from Paul 2015)

allowing the migration of chloride not only into the cracks, but also, subsequently, into the uncracked matrix between the cracks. Chloride from both the cracked and the uncracked parts were collected by means of drilling with a large (16 mm) diameter drill for the sampling and chloride profiling that was performed by Paul (2015).

The chloride diffusion Ingress Potential Index (IPI_{Cl}) that was derived from crack width distributions and chloride diffusion in cracks, as elaborated on in Sect. 2.2, as well as the unweighted *CWV*, which was also described in Sect. 2.2, were determined from the crack pattern data reported by Paul (2015) for the specimens of Series 1 and 2. Note that the chloride profiles were determined for twelve specimens in total, three specimens of Series 1 (FS2) and nine specimens of Series 2 (FS31), of which six after 37 weeks of cyclic chloride ponding and three after 57 weeks. The results obtained are presented in Fig. 2.21. From the graphs shown, a reasonable correlation was found with the total chloride content at the relatively low duration of exposure (37 weeks) for both of the indices involved (IPI_{Cl} and *CWV*). For longer exposure periods than the above, chloride has been found to continue to accumulate in the specimens. Such holds true even for the specimens of Series 1 that were exposed in the unloaded state, and which, thus, had relatively fine crack widths, as expressed by their lower IPI_{Cl} and *CWV* indices.

Whereas Fig. 2.21 indicates a degree of correlation between the crack distribution indices and the total chloride content, the IPI_{Cl} and *CWV* indices have not been derived or weighted for chloride ingress into non-saturated, cracked SHCC, as occurs in cyclic wetting and drying by means of ponding or capillary absorption of NaCl solution. For instance, the IPI_{Cl} incorporates a threshold crack width of 30 µm for steady-state chloride diffusion through water-filled parallel cracks (Boshoff et al. 2016; Djerbi et al. 2008). Below the threshold mentioned, no chloride passes through the cracks, while the steady-state diffusion is considered to be proportional to the crack width for crack widths between 30 and 100 µm, beyond which it remains constant. Further research is required to derive an ingress index that captures the mechanism of chloride ingress into flexural cracks in non-saturated SHCC more directly than above. Nevertheless, reasonable correlation is found

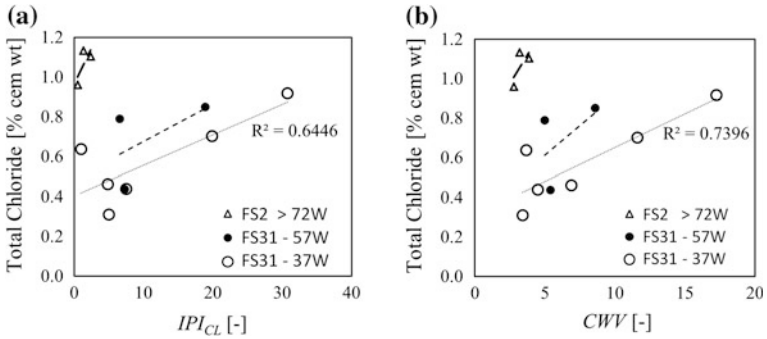

Fig. 2.21 Total chloride content (XRF) at the steel centre as function of **a** Ingress Potential Index (IPI_{Cl}), and **b** crack width value (CWV)

between the chloride content at the level of the steel bar in cracked SHCC and both the IPI_{Cl} and the CWV, for shorter exposure (37 weeks). In Chap. 9, test results of chloride-induced corrosion of rebar in the specimens (R/FS2, R/FS31) used are discussed, and the correlations between actual corrosion damage and the indices mentioned are investigated.

2.6 Capillary Absorption

Capillary absorption appears to be a frequently used criterion for the durability of cement-based materials. A high capillary absorption results in an accelerated ingress of deleterious substances. Under cyclic exposure, the substances can accumulate, over time, within the material. This is of particular importance for the ingress of chlorides.

Capillary absorption may be experimentally investigated by means of standardised test methods, such as according to DIN EN ISO 15148 (2003). It is usually assumed that the water uptake is proportional to the square root of the time t, and, accordingly, a so-called water absorption coefficient A is defined as follows:

$$A = \frac{x(t)}{\sqrt{t}} \cdot u_f \cdot \rho_{Solid} \tag{2.16}$$

with:

$x(t)$ the time-dependent penetration depth
u_f the maximum water content
ρ_{Solid} the dry density of the material

The capillary absorption of SHCC has been the subject of multiple investigations. Mechtcherine et al. (2007) reported on tests of undamaged and cracked

SHCC. The water absorption coefficient after 24 h was related to the total crack length, enabling a proportionality to be found. On the basis of the experimental results, deviations from the above-mentioned and generally accepted $\sqrt{t}$ dependence may be observed. Functions containing the fourth root of time allow for the improvement of fits to measured data, especially when long exposure times are considered. For ordinary concrete, deviations from the $\sqrt{t}$ dependence have been observed before.

In addition, Şahmaran and Li (2009) observed an increasing amount of water absorption, with an increasing damage level. The measured data also deviate from the above-mentioned $\sqrt{t}$ dependence. A linear relationship between water uptake and number of cracks could be shown. The application of a water-repellent admixture led to a significant reduction of the water absorption involved.

Zhang et al. (2010) were able to show, by means of the use of neutron radiography, that existing cracks, including those with small widths, at an SHCC surface subjected to capillary absorption become water-filled after only a few minutes and that, thereafter, the water penetrates from the cracks into the adjacent material. According to Wittmann et al. (2011), the effect is significantly reduced when the mortar matrix is hydrophobised by means of the use of a silane emulsion.

Similar observations were reported by Schröfl et al. (2015), who investigated the capillary absorption of RC beams with SHCC overlay (see Sect. 8.6). In addition to the fast water uptake of the cracks, the researchers concerned found an intensified capillary absorption for wider cracks.

The direct influence of crack distances on capillary absorption has not been the subject of the above-mentioned experimental observations. The influence concerned is of particular importance in the case of non-uniform crack spacing. Wagner (2016) conducted a test series aimed at separating individual contributions to capillary absorption, namely at detecting the capillary absorption of the undamaged SHCC surface, the water uptake of the cracks, and the capillary absorption of the rough crack surfaces. The crack spacing involved was believed to directly affect the overall absorption behaviour, since relatively narrow spaces between neighbouring cracks are likely to become saturated by water before wider ones are. In order to prove the assumption made, the tests that are schematically shown in Fig. 2.22 were conducted.

Below, the results obtained by Wagner (2016) are summarised. The absorbed water mass of the undamaged material appeared to be proportional to the fourth root of the exposure time. No essential difference was found between the mortars with and without fibres (see Fig. 2.23).

Figure 2.24a shows the expected linear relationship between the absorption coefficient after 24 h and the crack density, meaning the number of cracks per unit length. In Fig. 2.24b, it can be seen that the slope of the above-mentioned relationship decreases over the exposure time concerned. The decrease is attributed to the fact that the portion of the fully saturated spaces between neighbouring cracks increases.

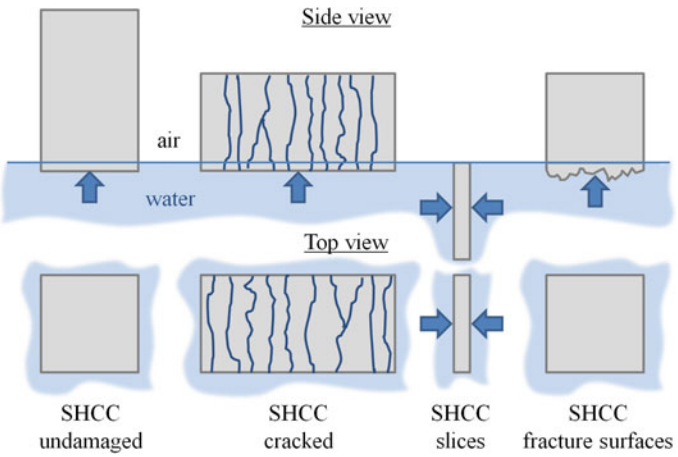

Fig. 2.22 Exposure conditions for capillary absorption tests (Wagner 2016)

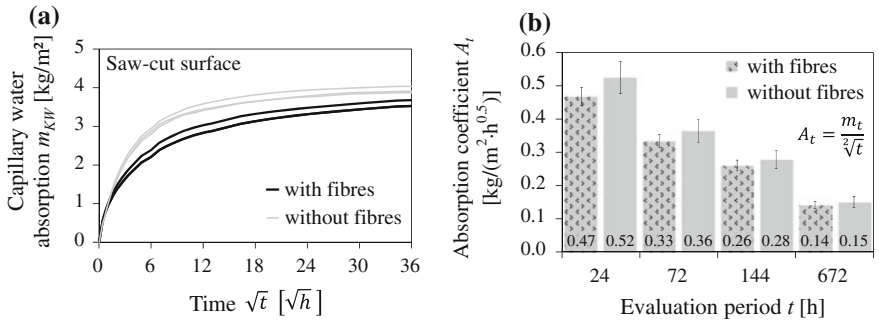

Fig. 2.23 **a** Water absorption of uncracked mortar versus time, and **b** absorption coefficient for different evaluation periods (Wagner 2016)

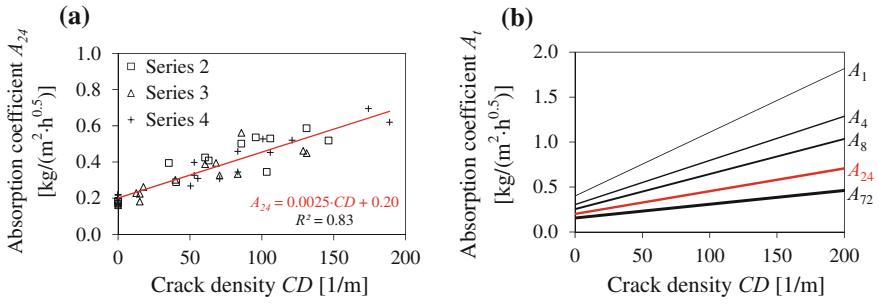

Fig. 2.24 Water absorption coefficient versus crack density for **a** an evaluation period of 24 h, and **b** for different evaluation periods (Wagner 2016)

The results for the capillary absorption of thin uncracked SHCC slices (see Fig. 2.22, third column) are presented in Fig. 2.25. At some point in time, depending on the slice thickness, it can clearly be seen that the water absorption is suddenly reduced. The reduction is due to the event reaching a state of water saturation.

The capillary absorption of fracture surfaces has also been investigated. In the tests concerned, the damage or micro-fracturing level of the surfaces was varied by means of using different fibre contents V_F. The higher the fibre content, the rougher or more micro-cracked the fracture surface is likely to be on the macroscopic scale. In Fig. 2.26a, it can be seen that the capillary absorption will be stronger for the rougher surfaces. The reasons for such an effect are the larger exposed surface area involved and, possibly, also the increased porosity due to micro-cracking. The diagram in Fig. 2.26b shows the capillary absorption coefficient A^{IV} for the case of proportionality to the fourth root of time. The influence of the fibre content, which is here assigned to a damage level D_F (see upper axis in Fig. 2.26b) can clearly be seen. The factor β_D, displayed in the same diagram, describes the relative increase of the capillary absorption coefficient with respect to the case of the fibreless mortar.

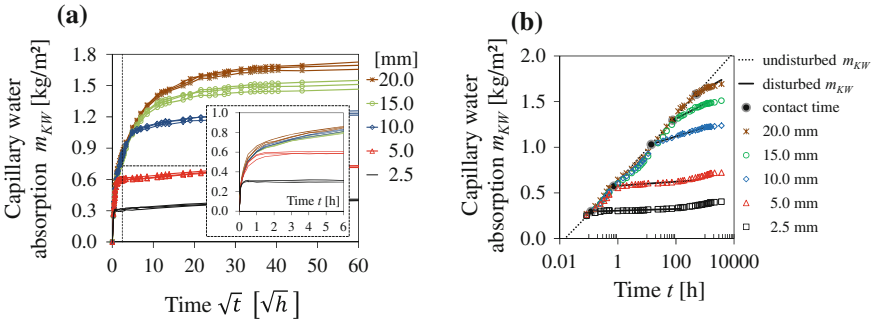

Fig. 2.25 Water absorption of thin SHCC slices (Wagner 2016)

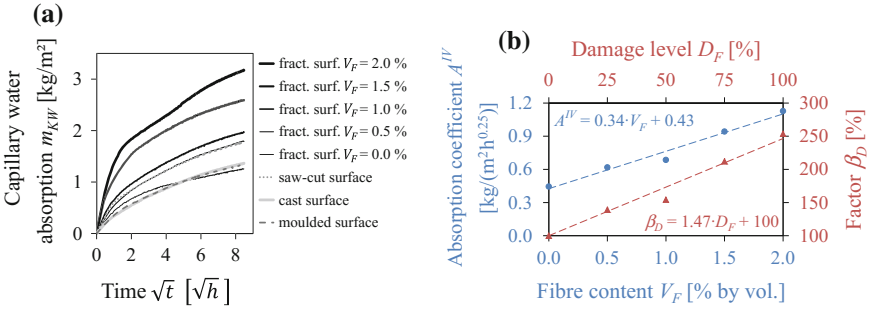

Fig. 2.26 Capillary absorption of fracture and reference surfaces (Wagner 2016)

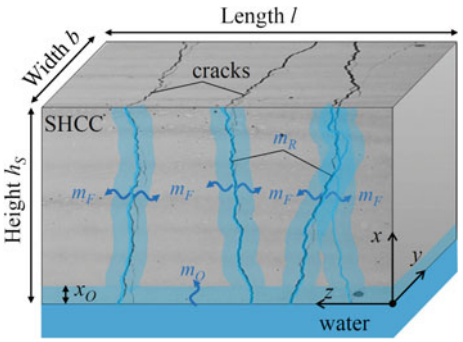

Fig. 2.27 Contributions to the capillary absorption of cracked SHCC (Wagner 2016)

The experimental observations formed the basis for the development of an analysis model in respect of the capillary absorption of porous materials with multiple closely spaced cracks (Wagner 2016). The above-mentioned three effects are schematically shown in Fig. 2.27. The different values m are always the absorbed mass per unit base area (at the lower surface).

The water uptake of the crack is denoted with m_R . By using the crack pattern parameters, as introduced in Sect. 2.2, including the class widths Δl and Δw, the following equation is obtained:

$$m_R = \frac{\rho_{Fluid} \cdot (\Delta l \cdot CLV) \cdot (\Delta w \cdot CWV) \cdot CD \cdot l \cdot h_S}{l \cdot b} \tag{2.17}$$

Note that m_R is independent of the exposure time involved. The independence is justified by the above-mentioned observation that the cracks are almost immediately water-filled after exposure.

For the capillary absorption of the fracture surfaces m_F, the following equation has been derived (Wagner 2016):

$$m_F(t) = \frac{\bar{A}_D^{IV} \cdot \overline{\beta_h}}{l \cdot b} \cdot \int_0^t \frac{1}{4} \cdot \tilde{t}^{-\frac{3}{4}} \cdot \beta_s(\tilde{t}) \cdot \overline{\beta_Q}(\tilde{t}) \cdot A_F(\tilde{t}) d\tilde{t} \tag{2.18}$$

with:

$$\mathrm{A}_D^{IV} = \mathrm{A}^{IV} \cdot \beta_D \text{ and } \beta_s(\tilde{t}) = \left(\frac{1}{1 - CSV \cdot \Delta s} + 1\right)^{\left(\frac{\left(\frac{2}{1-CSV\cdot\Delta s}+2\right)\cdot\bar{A}_D^{IV}}{u_f \cdot \rho_{trocken}} \cdot \sqrt[4]{\tilde{t}}\right)} \tag{2.19}$$

with:

A_D^{IV} the capillary absorption coefficient of the bulk material ("*IV*" for fourth root of time)

β_D the experimentally determined factor for the damage level of the fracture surfaces (see Fig. 2.26b)

$\beta_s(\tilde{t})$ a factor considering the experimentally determined crack spacing distribution *CSV* for a class width Δs

$\overline{\beta_Q}(\tilde{t})$ a factor considering the flow rate limited by the crack width

$\overline{\beta_H}$ a factor considering the changing pressure head along the crack

$A_F(\tilde{t})$ the crack surface area corrected for the penetration depth x_O at the lower surface (see Fig. 2.27)

The capillary absorption at the external (lower) surface may be calculated as follows:

$$m_O(t) = A^{IV} \cdot \int_0^t \frac{1}{4} \cdot \tilde{t}^{-\frac{3}{4}} \cdot \beta_s(\tilde{t}) \cdot d\tilde{t} \tag{2.20}$$

Finally, the theoretical total capillary absorption $m_{KW}^{th}(t)$ may be composed by means of applying the following equation:

$$m_{KW}^{th}(t) = m_O(t) + m_F(t) + m_R(t) \tag{2.21}$$

Similarly to the case of water permeability, the difference between the theoretical capillary absorption $m_{KW}^{th}(t)$ and the experimentally determined capillary absorption $m_{KW}^{exp}(t)$ may be quantified by means of the coefficient ξ_{KW}.

$$\xi_{KW} = \frac{m_{KW}^{exp}(t)}{m_{KW}^{th}(t)} \tag{2.22}$$

The reasons for the difference between theoretical and measured capillary absorption are the changing crack pattern parameters over the specimen depth, the existence of a nonconstant damage level along the crack length, and other deviations from the model simplifications. Figure 2.28 shows both the calculated and the

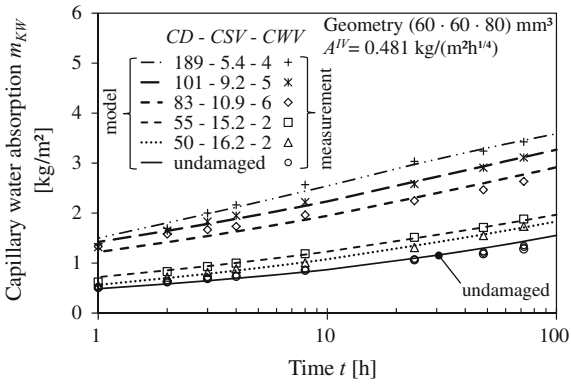

Fig. 2.28 Comparison of measured and calculated capillary water absorption of uncracked and cracked SHCC (Wagner 2016)

measured capillary absorption versus the exposure time. Fitting the calculated capillary absorption curves to the measured data yielded a coefficient $\xi_{KW} = 0.338$, with a standard deviation of 0.065.

2.7 Recommendations for Durability Design and Conclusions

The transport of different media through SHCC has been the subject of several experimental investigations. The relevant physical processes and the respective specifics of SHCC are known. In general, the crack patterns formed in the material appear to have a predominant influence on the transport rates and, if relevant, also on their dependence on exposure time. Hence, the combined action of mechanical loading and exposure to penetrating media has to be considered.

Methods for predicting the transport rates or for estimating the vulnerability to specific transport processes have been proposed. Some of the methods are empirical, others are based on known physical models, but all of them consider the influence of the actual crack pattern. Parameters were defined for describing and comparing the SHCC crack patterns. Such parameters may be determined on the basis of images of the respective cracked SHCC surfaces. In addition to the material properties, the type of the mechanical loading is affecting the formation of the crack pattern.

As far as chloride ingress is concerned, the proposed crack pattern parameters appear to be good indicators for shorter term ingress, and possibly even for corrosion initiation. But the accumulation of chloride in flexural cracks over time has not yet been correlated to these indices. This is partially due to limited experimental data being available and may provide further research opportunities in future. So far, no crack pattern parameter has yet been proposed that considers the crack depths as being of particular significance in relation to flexural loading.

The prediction of transport rates for certain exposure and loading conditions may form part of the durability design. An open issue, however, appears to be the quantification of the relationship between transport processes and structural durability. At the very least, critical values for the transport rates should be identified.

References

Boshoff, W.P., Adendorff, C.J. (2010). Modelling SHCC cracking for durability. V. Mechtcherine, M. Kaliske (eds.), Proceedings of a Symposium organized within the European Conference on Fracture (ECF-18), Aug. 30-Sept. 3, 2010, Dresden, Germany, Aedificatio Publishers, Freiburg, Germany, pp. 195-202.

Boshoff, W.P., Altmann, F., Adendorff, C.J., Mechtcherine, V. (2016). A new approach for modelling the ingress of deleterious materials in cracked strain hardening cement-based composites. Materials and Structures 49(6):2285-2295.

Clear, C.A. (1985). The effects of autogenous healing upon the leakage of water through cracks in concrete. Technical Report 559, Cement and Concrete Association.

DIN EN ISO 15148:2003-03 (2003). Wärme- und feuchtetechnisches Verhalten von Baustoffen und Bauprodukten – Bestimmung des Wasseraufnahmekoeffizienten bei teilweisem Eintauchen. Deutsches Institut für Normung, March 2003.

Djerbi, A., Bonnet, S., Khelidj, A., Baroghel-Bouny, V. (2008). Influence of traversing crack on chloride diffusion into concrete. Cement and Concrete Research 38(6):877-883.

DuraCrete (2000). Probabilistic performance based durability design of concrete structures. Report R15, 2000, Project BE95-1347, The European Union – Brite Euram III.

Edvardsen, C.K. (1996). Wasserdurchlässigkeit und Selbstheilung von Trennrissen in Beton. Deutscher Ausschuss für Stahlbeton, Heft 455, Beuth Verlag, Berlin, Germany.

Kobayashi, K., Iizuka, T., Kurachi, H., Rokugo, K. (2010). Corrosion protection performance of high performance fibre reinforced cement composites as a repair material. Cement and Concrete Composites 32(6):411-420.

Kojima, Y., Dung, L.A., Rokugo, K., Kobayashi, K. (2014). Chloride proofing and rebar corrosion proofing performances of SHCC having cracks. E. Schlangen, M.G. Sierra Beltran, M. Luković, G. Ye (eds.), Proceedings of the 3rd International RILEM Conference on Strain Hardening Cementitious Composites, 3-5 November 2014, Dordrecht, The Netherlands, RILEM Publications S.A.R.L., Bagneux, France, pp. 61-68.

Lepech, M.D., Li, V.C. (2009). Water permeability of engineered cementitious composites. Cement and Concrete Composites 31(10):744-753.

Mechtcherine, V., Lieboldt, M., Altmann, F. (2007). Preliminary tests on air-permeability and water absorption of cracked and uncracked strain hardening cement-based composites. K. Audenaert, L. Marsavina, G. de Schutter (eds.), Proceedings of the International RILEM Workshop on Transport Mechanisms in Cracked Concrete, Ghent, Belgium, 7 September 2007, Acco, Leuven, Belgium, pp. 55-66.

Mechtcherine, V., Lieboldt, M. (2011). Permeation of water and gases through cracked textile reinforced concrete. Cement and Concrete Composites 33(7):725-734.

Moukwa, M (1990). Deterioration of concrete in cold sea waters. Cement and Concrete Research 20(3):439-446.

Paul, S.C., Van Zijl, G.P.A.G. (2014). Crack formation and chloride induced corrosion in reinforced strain hardening cement-based composite (R/SHCC). Journal of Advanced Concrete Technology 12:340-351.

Paul, S.C. (2015). The role of cracks and chloride in corrosion of reinforced strain hardening cement-based composite (R/SHCC). PhD Thesis, Stellenbosch University, South Africa.

Paul, S.C., Van Zijl, G.P.A.G., Babafemi, A.J., Tan, M.J. (2016). Chloride ingress in cracked and uncracked SHCC under cyclic wetting-drying exposure. Construction and Building Materials 114:232-240.

RILEM TC 178-TMC (2002a). Testing and modelling chloride penetration in concrete, Analysis of total chloride content in concrete. Materials and Structures 35(9):583-585.

RILEM TC 178-TMC (2002b). Testing and modelling chloride penetration in concrete, Analysis of water soluble chloride content in concrete. Materials and Structures 35(9):586-588.

Ripphausen, B. (1989). Untersuchung der Wasserdurchlässigkeit und Sanierung von Stahlbetonbauteilen mit Trennrissen. Doctoral thesis, RWTH Aachen, Germany.

Şahmaran, M., Li, V.C. (2009). Influence of microcracking on water absorption and sorptivity of ECC. Materials and Structures 42(5):593-603.

Schröfl, C., Mechtcherine, V., Kaestner, A., Vontobel, P., Hovind, J., Lehmann, E. (2015). Transport of water through strain-hardening cement-based composite (SHCC) applied on top of cracked reinforced concrete slabs with and without hydrophobization of cracks – Investigation by neutron radiography. Construction and Building Materials 76:70-86.

Tsukamoto, M., Fiebrich, M (1994). Untersuchung zur Durchlässigkeit von faserfreien und faserverstärkten Betonbauteilen mit Trennrissen. Deutscher Ausschuss für Stahlbeton, Heft 440, Beuth Verlag, Berlin, Germany.

Van Zijl, G.P.A.G., Slowik, V., Toledo Filho, R.D., Wittmann, F.H., Mihashi, H. (2016). Comparative testing of crack formation in strain-hardening cement-based composites (SHCC). Materials and Structures 49(4):1175-1189.

Wagner, C., Bretschneider, N., Slowik, V. (2011). Evaluation of crack patterns in strain hardening cement-based composites (SHCC) with respect to structural durability. Restoration of Buildings and Monuments 17(3/4):223-237.

Wagner, C., Slowik, V. (2011). On the water permeability of cracked strain hardening cement-based composites. R.D. Toledo Filho, F.A. Silva, E.A.B. Koenders, E.M.R. Fairbairn (eds.), Proceedings of the 2nd International RILEM Conference on Strain Hardening Cementitious Composites (SHCC2), 12-14 December 2011, Rio de Janeiro, Brazil, RILEM Proceedings (PRO 81), RILEM Publications S.A.R.L., Bagneux, France, pp. 181-188.

Wagner, C., Dollase, A., Slowik, V. (2012). Evaluation of crack patterns in SHCC with respect to water permeability and capillary suction. M.G. Alexander (ed.), Proceedings of the 3rd International Conference on Concrete Repair, Rehabilitation and Retrofitting (ICCRRR), 3-5 September 2012, Cape Town, South Africa, CRC Press, Leiden, The Netherlands, pp. 972-977.

Wagner, C. (2016). Dauerhaftigkeitsrelevante Eigenschaften von dehnungsverfestigenden zementgebundenen Reparaturschichten auf gerissenen Betonuntergründen (Durability related properties of strain hardening cement-based repair layers on cracked concrete substrates). Doctoral thesis, Technische Universität Dresden, Germany.

Wang, K., Jansen, D.C., Shah, S.P., Karr, A.F. (1997). Permeability study of cracked concrete. Cement and Concrete Research 27(3):381-393.

Wittmann, F.H., Wang, P., Zhang, P., Zhao, T., Beltzung, F. (2011). Capillary absorption and chloride penetration into neat and water repellent SHCC under imposed strain. R.D. Toledo Filho, F.A. Silva, E.A.B. Koenders, E.M.R. Fairbairn (eds.), Proceedings of the 2nd International RILEM Conference on Strain Hardening Cementitious Composites (SHCC2-Rio), 12-14 December 2011, Rio de Janeiro, Brazil, RILEM Proceedings (PRO 81), RILEM Publications S.A.R.L., Bagneux, France, pp. 165-172.

Wittmann, F.H., Zhang, P., Zhao, T. (2012). Importance of water repellent treatment of SHCC for durability and service life. Restoration of Buildings and Monuments 18(1):31-40.

Yeomans, S.R. (2004). Galvanized steel reinforcement in concrete. Elsevier Science, Amsterdam, The Netherlands.

Zhang, P., Wittmann, F.H., Zhao, T., Lehmann, E.H. (2010). Neutron imaging of water penetration into cracked steel reinforced concrete. Physica B: Condensed Matter 405 (7):1866-1871.

Springer

http://www.springer.com/978-94-024-1012-9

A Framework for Durability Design with Strain-Hardening Cement-Based Composites (SHCC)
State-of-the-Art Report of the RILEM Technical Committee 240-FDS
van Zijl, G.P.A.G.; Slowik, V. (Eds.)
2017, XX, 200 p. 123 illus., Hardcover
ISBN: 978-94-024-1012-9